

1 **Turbulence measurements from compliant moorings - Part II: motion**
2 **correction**

3 Levi Kilcher*, Jim Thomson, Samuel Harding and Sven Nylund

4 * *Corresponding author address:* National Renewable Energy Laboratory, Golden, Colorado

5 E-mail: Levi.Kilcher@nrel.gov

ABSTRACT

6 Acoustic Doppler velocimeters (ADV) are a valuable tool for making high-
7 precision measurements of turbulence, and moorings are a convenient and
8 ubiquitous platform for making many kinds of measurements in the ocean.
9 However—probably due to concerns that mooring motion can contaminate
10 turbulence measurements, and because acoustic Doppler profilers are rela-
11 tively easy to deploy—ADVs are not frequently deployed from moorings.
12 This work details a method for measuring turbulence using moored acoustic
13 Doppler velocimeters (ADVs) that corrects for mooring motion using mea-
14 surements from inertial motion sensors (IMUs). Three distinct mooring plat-
15 forms are deployed in a tidal channel with IMU-equipped ADVs. In each case
16 the inertial measurements dramatically reduce contamination from mooring
17 motion. The spectra from these measurements have a shape that is consistent
18 with other measurements in tidal channels, and have a $f^{-5/3}$ slope at high
19 frequencies—consistent with Kolmogorov’s theory of isotropic turbulence.
20 Motion correction also improves estimates of cross-spectra and Reynold’s
21 stresses. Comparison of turbulence dissipation with flow speed and turbulence
22 production indicates a bottom boundary layer production-dissipation balance
23 during ebb and flood that is consistent with the strong tidal forcing at the site.
24 These results indicate that IMU-equipped ADVs are a valuable new tool for
25 measuring turbulence from moorings.

26 1. Introduction

27 Acoustic Doppler velocimeters (ADV) have been used to make high-precision measurements
28 of water velocity for over 20 years (Kraus et al. 1994; Lohrmann et al. 1995). During that time they
29 have been deployed around the world to measure turbulence from a range of platforms, including:
30 stationary structures on ocean- and lake-bottoms, in surface waters from a pole lowered from
31 a ship’s bow, and in the deep ocean from autonomous underwater vehicles (e.g. Voulgaris and
32 Trowbridge 1998; Zhang et al. 2001; Kim et al. 2000; Goodman et al. 2006; Lorke 2007; Geyer
33 et al. 2008; Cartwright et al. 2009).

34 A relatively small fraction of ADV measurements have been made from moorings (e.g. Fer
35 and Paskyabi 2014). Presumably this is because mooring motion can contaminate ADV mea-
36 surements, and acoustic Doppler *profilers* (ADPs) can be used to measure mid-depth turbulence
37 statistics without a mooring (e.g. Stacey et al. 1999a; Rippeth et al. 2002; Wiles et al. 2006). Still,
38 ADV measurements have distinct characteristics that can be advantageous: they are capable of
39 higher sample-rates, they have higher signal-to-noise ratios, and they have a much smaller sample-
40 volume (1 centimeter, as opposed to several meters). That is, compared to an ADP, ADVs are high
41 precision instruments capable of providing unique information. They could be more widely used
42 as a moored-instrument (i.e. at arbitrary depth) if a method for accounting for mooring motion can
43 be demonstrated to provide more accurate estimates of turbulence statistics.

44 Inertial motion sensors (IMUs) have been used in the aerospace and aeronautical industries to
45 quantify the motion of a wide range of systems—including aircraft, rockets, and spacecraft—for
46 several decades, but their cost has come down as their market has grown beyond these niche sectors
47 (Bevly 2004). Over the last ten years massive growth in the smart-phone, drone, and ‘Internet
48 of Things’ markets has driven innovation in micro-electrical-mechanical systems (MEMS). One

49 component that has emerged from this sector is the IMU. Also known as ‘Magnetic, angular-rate,
50 gravity’ (MARG), or ‘attitude heading reference system’ (AHRS) sensors, IMUs measure three
51 axes of: the earth’s magnetic field, angular rotation, and linear acceleration. These signals are then
52 integrated using Kalman filters to estimate the orientation and motion of the sensor (Barshan and
53 Durrant-Whyte 1995; oáo Luis Marins et al. 2001; Bachmann et al. 2003)¹.

54 Nortek now offers a version of their Vector ADV with a Microstrain 3DM-GX3-25 IMU sen-
55 sor (Nortek 2005; MicroStrain 2012). The IMU’s signals are incorporated into the Vector data
56 stream so that the motion and orientation signals are tightly synchronized with the ADV’s velocity
57 measurements. This tight synchronization provides a data-stream that can be utilized to quan-
58 tify ADV motion in the earth’s inertial reference frame, and remove that motion from the ADV’s
59 velocity measurements at each time-step of its sampling. This work provides a detailed account-
60 ing for performing motion correction of these ‘ADV-IMU’ measurements, and presents results
61 of this method using data from a range of mooring configurations that positioned ADV-IMUs at
62 mid-depths in Puget Sound.

63 This effort was originally motivated by a need for low-cost, high-precision turbulence measure-
64 ments for the emerging tidal energy industry (McCaffrey et al. 2015; Alexander and Hamlington
65 2015). Experience in the wind energy industry has shown that wind turbine lifetime is reduced
66 by atmospheric turbulence, and the same is expected to be true for tidal energy turbines. In wind,
67 meteorological towers are often used to position sonic anemometers at the hub-height of wind
68 turbines for measuring detailed turbulence inflow statistics (Hand et al. 2003; Kelley et al. 2005;
69 Mücke et al. 2011; Afgan et al. 2013). In the ocean, tower-mounted hub-height turbulence mea-
70 surements have been made, but they are challenging to install and maintain in energetic tidal sites

¹Within this literature, ‘IMU’ is generally reserved for a MARG sensor without a magnetometer, but herein we refer to the entire group of sensors that measure motion using accelerometers and angular-rate sensors as ‘IMUs’.

71 (Gunawan et al. 2014). Thus, the Department of Energy funded this work to investigate the ac-
72 curacy of mooring deployed ADV-IMUs to reduce the cost of turbulence measurements at tidal
73 energy sites (Kilcher et al. 2016). The approach proved to be successful and potentially useful to
74 the broader oceanographic community interested in moored turbulence measurements (Lueck and
75 Huang 1999; Doherty et al. 1999; Nash et al. 2004; Moum and Nash 2009; Alford 2010; Paskyabi
76 and Fer 2013).

77 The next section describes details of the measurements, including a summary of the hardware
78 configurations (platforms) that were used to support and position the ADV-IMUs in the water-
79 column. A detailed description of the motion of these platforms is found in the companion paper to
80 this work, Harding et al. (2017), hereafter ‘Part 1’. Section 3 describes the mathematical details of
81 motion correction, and section 4 presents results from application of the method to measurements
82 from the various platforms. Section 5 is a discussion of the energetics of the tidal channel where the
83 measurements were made and demonstrates that the measurements are consistent with turbulence
84 theory and other measurement in similar regimes. A summary and concluding remarks is found in
85 section 6.

86 **2. Measurements**

87 This work is focused on measuring turbulence from ADVs that are deployed from non-stationary
88 platforms and equipped with inertial motion sensors (IMU). The ADVs utilized for these measure-
89 ments were all equipped with Microstrain 3DM-GX3-25 IMU sensors that captured all 6 compo-
90 nents of the ADV motion (3 components of angular rotation and 3 components of linear acceler-
91 ation), as well as the orientation of the ADV pressure-case. The sampling of the motion sensor is
92 tightly synchronized with the ADV measurements. The IMU measures its motion at 1kHz and uses
93 internal signal integration (Kalman filtering) to output the motion signals at the same sample rate

94 as the ADV's velocity measurements. This reduces aliasing of the IMU's motion measurements
95 above the ADV's sample-rate (MicroStrain 2010). Cable-head ADVs were utilized throughout
96 this work to allow for flexibility in the positioning of the ADV head relative to its pressure case.

97 All measurements used in this work were made in Admiralty Inlet, Washington, approximately
98 500 meters (m) WSW of Admiralty Head–Fort Casey State Park—in 60 m of water depth at latitude
99 48.153 north and longitude 122.687 west (Figure 1). The site is approximately 6 kilometers (km)
100 east of Port Townsend, and 1 km north of the Port Townsend – Coupeville ferry route. Admiralty
101 inlet is the largest waterway connecting Puget Sound to the Strait of Juan de Fuca, and it possesses
102 a large semi-diurnal tidal flow. This work utilizes data from three distinct deployment platforms:
103 the 'tidal turbulence mooring', a 'StableMoor' buoy, and a simple sounding weight. Additional
104 details, photos, and schematic diagrams of all three mooring systems can be found in Part 1.

105 *a. Tidal Turbulence Mooring (TTM)*

106 The 'tidal turbulence mooring' (TTM) is a simple mooring system with a 'strongback fin' sus-
107 pended between a steel clump-weight anchor weighing 1200 kilograms (kg) when dry and a 0.93
108 m-diameter spherical steel buoy with a buoyancy of 320 kg. The ADV pressure cases were
109 clamped to one side of the strongback fin and the ADV sensor head was positioned 10 cm in
110 front of the fin's leading edge (Figure 2). The leading edge of the fin is fastened inline with the
111 mooring line. This configuration was designed to work similar to a weather-vane, such that the
112 drag on the fin held the ADV head upstream of the mooring components. This work utilizes data
113 from two TTM deployments.

114 1) JUNE 2012 TTM DEPLOYMENT

115 The first was in June of 2012 at 48.15285 north, 122.68581 west. The mooring was in the water
116 from 17:30 on the 12th until 14:30 on the 14th (local, i.e. pacific daylight time). Two Nortek
117 ADVs were clamped to either side of the fin such that the axis of their cylindrical pressure-cases
118 were parallel with the leading edge of the strongback. The ADV heads were spaced 0.5 m apart
119 vertically along the fin. Only one of these ADVs was equipped with an integrated IMU. This TTM
120 also had an upward-looking acoustic Doppler profiler mounted on the mooring anchor.

121 Periods of time during which this mooring interfered with a beam of the Doppler profiler were
122 identified by inspection of the profiler's acoustic amplitude signal. Periods during which one
123 beam of the profiler had $> 5\%$ higher acoustic amplitude than the other beams were flagged as
124 'contaminated' and excluded from averaging. 5-minute averages in which more than 50% of the
125 data was contaminated in this way were masked as invalid.

126 2) JUNE 2014 TTM DEPLOYMENT

127 The second TTM deployment was in 2014 from 06:00 on June 17 to 05:00 on June 19 (local
128 time). The mooring was positioned at 48.15327 north, 122.68654 west. Two Nortek ADV-IMUs
129 were mounted on this TTM, with their heads spaced 0.5 m apart along the fin. In this case the
130 pressure-cases and ADV heads were inclined at an angle of 18° to the leading edge of the fin
131 to account for mooring blow-down during strong currents (Figure 3). This change was made
132 to reduce vibrational motion observed during the June 2012 deployment that was believed to be
133 associated with the orientation of the pressure cases.

b. The StableMoor platform

The second deployment platform was a cylindrical, ‘StableMoor’, syntactic foam buoy (manufacturer: Deep Water Buoyancy) that was anchored to a clump weight that weighed 2700 lbs (Figure 4). The buoy is 3.5 m long and 0.45 m in diameter with a tail ring that is 0.76 m in diameter. The StableMoor weighs 295 kg in air, and has a buoyancy of 185 kg in water.

The StableMoor was ballasted to pitch upward a few degrees in zero-flow to avoid ‘flying downward’. In the presence of an oncoming current the tail fins help to orient it into the flow. The anchor for this buoy is similar to that of the TTM, including an acoustic release so the mooring and anchor can be recovered separately.

The StableMoor platform has two primary advantages compared to the TTM. First, it is significantly more massive and hydro-dynamically stable than the TTM, which reduces the frequency of motions of the platform. The other major advantage of the StableMoor platform is that it is capable of supporting a bottom-tracking acoustic Doppler profiler, which provides an independent measure of the platform’s translational motion. Disadvantages of the StableMoor include: a) its size adds to the challenge of deployment and recovery, and b) it is significantly more expensive than the TTM system.

The StableMoor was deployed with an ADV-IMU mounted at its nose from 11:21 on May 12 to 11:53 on May 13, 2015 (local time). This deployment was at 48.15277 north, 122.68623 west. In this configuration the sample volume of the ADV is 10 cm forward of the nose and 20 cm above the centerline of the StableMoor (Figure 4). Based on Wyngaard et al.’s (1985) investigation of a similarly shaped slender body the velocity measurements should have flow-distortion effects of less than 10%. This configuration was designed to be the most stable platform for measuring turbulence from a moving platform. The StableMoor was equipped with a 1200 kHz RDI workhorse

157 sentinel acoustic Doppler profiler that was oriented downward-looking to measure water velocity
158 below the platform in 12 1-meter bins and measure buoy motion (‘bottom tracking’), all at a 1 Hz
159 sample rate.

160 *c. Turbulence Torpedo*

161 The turbulence torpedo is a simple sounding weight with an ADV head mounted forward of the
162 nose, and the ADV pressure case strapped below. This platform was deployed on May 14, 2015
163 for 37 minutes starting at 07:41 local time. This measurement was made from a davit that hung
164 the system from the side of the ship to a depth of approximately 25 m. The primary logistical
165 advantages of this platform are its compact size, low cost, and the flexibility to perform spatial
166 transects.

167 *d. Coordinate system and turbulence averaging*

168 Unless stated otherwise, vector quantities in this work are in a fixed ‘principal-axes’ coordinate
169 system that is aligned with the bi-directional tidal flow: positive u is in the direction of ebb (310°
170 True), positive w is vertically upward, and v is the cross-stream component in a right-handed
171 coordinate system. The full velocity vector, $\vec{u} = (\tilde{u}, \tilde{v}, \tilde{w})$, is separated into a mean and turbulent
172 component as $\vec{u} = \bar{\vec{u}} + \vec{u}$, where the over-bar denotes a 5 minute average. Turbulence kinetic
173 energy, $\text{tke} = \overline{u^2} + \overline{v^2} + \overline{w^2}$, and Reynold’s stresses, \overline{uv} , \overline{uw} , \overline{vw} are computed by averaging over the
174 5-minute window. Throughout this work we use $\bar{U} = (\bar{u}^2 + \bar{v}^2)^{1/2}$ to denote the mean horizontal
175 velocity magnitude.

176 All spectra, $S\{x\}(f) = |\mathcal{F}\{x(t)\}|^2$, and cross-spectra, $C\{x, y\}(f) = \text{real}(\mathcal{F}\{x(t)\}\mathcal{F}\{y(t)\})$, are
177 computed using NumPy fast Fourier transform routines (van der Walt et al. 2011). Here, $\mathcal{F}\{x(t)\}$

denotes the fast Fourier transform of a signal $x(t)$. Time series', e.g. $x(t)$, are linearly detrended and Hanning windowed prior to computing $\mathcal{F}\{x\}$ to reduce spectral reddening.

Throughout the remainder of this work the dependence of S and C on f is implied (e.g. $S\{x\}(f)$ is hereafter $S\{x\}$), and for other variables the dependence on t is implied. Spectra and cross-spectra are normalized to preserve variance: $\int S\{u\}df = \overline{u^2}$, and $\int C\{u, v\}df = \overline{uv}$. The notations $S\{\vec{u}\} = (S\{u\}, S\{v\}, S\{w\})$ and $C\{\vec{u}\} = (C\{u, v\}, C\{u, w\}, C\{v, w\})$ denote the set of spectra and cross-spectra for each velocity component and pairs of components, respectively.

Turbulence dissipation rates are computed as,

$$\varepsilon = \frac{1}{\overline{U}} \left(\alpha \left\langle (S\{u\} + S\{v\} + S\{w\}) f^{5/3} \right\rangle_{f_{IS}} \right)^{3/2} \quad (1)$$

Where $\alpha = 0.5$, and $\langle \rangle_{f_{IS}}$ denotes an average over the inertial-subrange of the velocity spectra and where the signal-to-noise ratio is small (Lumley and Terray 1983; Sreenivasan 1995). Throughout this work we take this average from 0.3 to 1 Hz for the u and v components, and 0.3 to 3 Hz for the w component.

3. Methodology

The essential approach of motion correction is to estimate time-series of velocity on a compliant mooring by obtaining an independent estimate of ADV head motion and removing that motion from the measured signal. Previous works have utilized inertial motion sensors to quantify the motion of 'multi-scale profilers' for the purpose of measuring the full spectrum of oceanic shear (Winkel et al. 1996). Nortek's ADV-IMU measures the linear acceleration, \vec{a} , rotational-motion, $\vec{\omega}$, and orientation matrix, \mathbf{R} , of the ADV pressure case (body) in the earth reference frame. So long as the ADV head is rigidly connected to the ADV pressure case, it is possible to utilize the IMU motion signals to calculate the motion of the ADV head, and remove it from the measured

velocity signal (Miller et al. 2008). The ADV head motion, is calculated as the sum of rotational and translational motion:

$$\begin{aligned}\vec{u}_h &= \vec{u}_\omega + \vec{u}_a + \vec{u}_{low} \\ &= \mathbf{R}^T \cdot \vec{\omega}^*(t) \times \vec{\ell}^* + \int \{\vec{a}(t)\}_{HP(f_a)} dt + \vec{u}_{low}\end{aligned}\tag{2}$$

Here ‘*’ superscripts denote quantities in the ADV’s local coordinate system, and $\vec{\ell}^*$ is the vector from the IMU to the ADV head. \mathbf{R}^T —the inverse of the orientation matrix—rotates vectors from the IMU to the earth reference frame. The notation $\{\vec{a}\}_{HP(f_a)}$ indicates that the IMU’s accelerometer signal is high-pass filtered (in the earth’s stationary reference frame) at a chosen filter-frequency, f_a . This is necessary because accelerometers have low-frequency noise, sometimes referred to as ‘bias-drift’ (Barshan and Durrant-Whyte 1995; Bevy 2004; Gulmammadov 2009).

Integrating \vec{a} to estimate \vec{u}_a amplifies the bias-drift noise at low-frequencies, which dramatically reduces the signal-to-noise ratio at those time scales (Figure A1). The high-pass filtering reduces this noise so that it does not contaminate motion correction, but real motion that exists at these frequencies is still lost in the low signal-to-noise ratio (Egeland 2014; VanZwieten et al. 2015). This means that low-frequency motion is not well resolved by the IMU, and so there is a residual low-frequency translational motion, \vec{u}_{low} , that needs to be measured independently—or at the very least considered—when using motion corrected ADV-IMU data. The $\vec{\omega}$ and \vec{u}_ω estimates do not have the same issue because there is no integration involved, and because low-frequency bias-drift in the $\vec{\omega}$ sensors is stabilized by the IMU’s on-board Kalman filtering (i.e. the accelerometer and magnetometer signals provide estimates of down and North, respectively, which stabilize orientation estimates and eliminates bias from rotation estimates).

The choice of high-pass filter for reducing low-frequency accelerometer noise depends on the flow conditions of the measurement, and the platform that is being used. In particular, filter-selection involves a trade off between filtering-out the bias-drift noise while not filtering-out

measured motion that is unresolved by an independent measurement of \vec{u}_{low} . If an independent measure of low-frequency motion is available it can be used to increase the accuracy of \vec{u}_{h} at low-frequency. Note that, to avoid double counting, \vec{u}_{low} should be estimated by applying the complimentary low-pass filter to the independent measurement of low-frequency motion.

With this estimate of ADV head motion it is straightforward to correct the measured velocity, \vec{u}_{m} , to estimate the velocity in the earth’s inertial reference frame:

$$\vec{u}(t) = \vec{u}_{\text{m}}(t) + \vec{u}_{\text{h}}(t) \quad . \quad (3)$$

Note here that the ‘+’-sign is correct because head motion, \vec{u}_{h} , induces a measured velocity in the opposite direction of the head motion itself ($\vec{u}_{\text{m}} = \vec{u} - \vec{u}_{\text{h}}$).

For the TTM and Turbulence Torpedo we utilize $f_a = 0.0333\text{Hz}$ (30 second period), and assume that $\vec{u}_{\text{low}} = 0$. For the StableMoor $f_a = 0.2\text{Hz}$ (5 second period). The bottom-track velocity was low-pass filtered at this frequency to provide an estimate of \vec{u}_{low} , and \vec{a} was high-pass filtered at this frequency. We use 4-pole, bi-directional (zero-phase), Hanning filters for all filtering operations.

Additional details on motion correction—including a detailed accounting of the distinct coordinate systems of the IMU, ADV pressure case, and ADV head—can be found in Kilcher et al. (2016). Open-source Python tools for performing motion correction of ADV-IMU data—including scripts that write processed data in Matlab and tabulated formats—are available at <http://lkilcher.github.io/dolfyn/>.

4. Results

a. Mean velocity

Figure 7 shows a comparison of \vec{u} measured by an ADV-IMU mounted on a TTM, to that of an upward-looking acoustic Doppler profiler mounted on the TTM anchor. This shows excellent

242 agreement between the ADV and Doppler profiler measurements of velocity. The \bar{u} , \bar{v} and \bar{w}
243 components have a root-mean-square error of 0.05, 0.13 and 0.03 m/s, respectively. While it
244 is important to note that there is some discrepancy between ADP and ADV measured velocities
245 (especially in \bar{v} , which is most likely due to incomplete motion correction), the agreement between
246 the magnitude and direction of these independent velocity measurements indicates that moored
247 ADV-IMUs provide a reliable estimate of velocity in the Earth's reference frame.

248 *b. TTM spectra*

249 As discussed in detail in Part 1 the mooring motion of the TTM, $S\{\bar{u}_h\}$, has a peak at 0.1 to 0.2
250 Hz from swaying of the mooring that is most likely driven by eddy-shedding from the spherical
251 buoy (Figure 8, red lines). There is also higher-frequency broad-band motion that is associated
252 with fluttering of the strongback fin around the mooring line. Both of these motions are especially
253 energetic in the v -component spectra, because this is the direction in which the TTM mooring
254 system is most unstable. As is expected from fluid-structure interaction theory the amplitude of
255 these motions increases with increasing mean velocity (Morison et al. 1950).

256 The mooring motion contaminates the uncorrected ADV-measurements of velocity, $S\{\bar{u}_m\}$,
257 whenever the amplitude of the motion is similar to or greater than the amplitude of the turbulence.
258 Fortunately, much of this motion can be removed using the IMU's motion signals as detailed in
259 section 3. Lacking an independent measurement of turbulence velocity at this site, we interpret the
260 agreement of these spectra with turbulence theory and as evidence of the success of the method.
261 In particular, at high-frequencies ($f > 0.3$ Hz) for each mean-flow speed the spectra decay with
262 a $f^{-5/3}$ slope and have equal amplitude across the velocity components. These results are con-
263 sistent with Kolmogorov's (1941) theory of isotropic turbulence, and are consistent with spectral

shapes of earlier measurements of turbulence in energetic tidal channels from stationary platforms (Kolmogorov 1941; Walter et al. 2011; Thomson et al. 2012; McMillan et al. 2016).

For $|\vec{u}| > 1.0$, motion correction modifies the u and v component spectra at frequencies as high as 3Hz. This indicates that in order for motion correction to be effective, synchronization between the ADV and IMU needs to be within 1/3 second or better. This suggests that asynchronous approaches to motion correction may be challenging, especially considering that the clock-drift of some instrumentation can be as high as a few seconds per day. By integrating the IMU data into the ADV data stream, the Nortek IMU-ADV achieves a synchronization to within 1e-2 seconds.

At low frequencies, the spectra tend to become roughly constant (especially at higher flow speeds), which is also consistent with previous works. Note here, that the very-low magnitude of $S\{\vec{u}_h\}$ at low frequencies is partially a result of filtering the IMU's accelerometer signal when calculating \vec{u}_a . The true low-frequency spectrum of ADV-head motion is unknown (indicated using a dashed line below f_a). A comparison of $S\{\vec{u}\}$ measured by the TTM to that measured by the ADP—during the June 2012 deployment—are in agreement at low-frequencies (not shown). This suggests that the assumption that $\vec{u}_{low} = 0$ at these frequencies, at this site, for this platform is justified—even if $S\{\vec{u}_h\}$ is not as low as indicated in Figure 8.

As successful as motion correction is, some of the motion contamination persists in $S\{\vec{u}\}$. This is most notable in $S\{v\}$ at the highest flow speeds (> 2.0 m/s): a peak at 0.15 Hz is an order of magnitude larger than a spectral fit to the other frequencies would indicate. This persistent motion contamination is evident to a lesser degree in $S\{u\}$ for $|u| > 2$ m/s, and in $S\{v\}$ at lower flow speeds. $S\{w\}$ appears to have no persistent motion contamination because the amplitude of the motion in this direction is much lower than for the other two components. For these measurements, $S\{w_h\}$ is so low that w -component motion correction is only necessary when $|u| > 2$ m/s.

287 The amplitude of the persistent motion contamination peaks in $S\{v\}$ at 0.15 Hz are a factor of 5 to
288 10 times smaller than the amplitude of the ADV head motion itself. This suggests the Microstrain
289 IMU can be used to effectively correct for mooring motion at 0.15 Hz when the amplitude of that
290 motion is less than 3 times the amplitude of the real turbulence spectrum. Where we have chosen
291 a value of 3 as a conservative estimate of motion correction's effectiveness.

292 This reveals an ancillary benefit of the IMU measurements: in addition to the primary benefit of
293 correcting for mooring motion, they can also be used to identify and screen-out persistent motion
294 contamination. For example, one of the most common uses of turbulence spectra is for the calcu-
295 lation of ϵ and tke . For these purposes, based on the relative amplitudes of the 0.15 Hz peaks, we
296 assume that persistent motion contamination is likely where $S\{\vec{u}_h\}/S\{\vec{u}\} > 3$ and exclude these
297 regions from spectral fits.

298 In the present case, for the u and w spectra, this criteria only excludes a narrow range of frequen-
299 cies at the 0.15 Hz motion peak for some cases. This criteria is more restrictive of the v -component
300 spectra at high frequencies for $\bar{U} > 1.0$ m/s, but this may be acceptable because the amplitude of
301 the spectrum at these frequencies—i.e. in the isotropic inertial subrange—should be equal to that
302 of u and w (Kolmogorov 1941).

303 Agreement of the v -component spectral amplitude with that of u and w at frequencies > 0.3
304 Hz indicates that motion correction is effective at those frequencies even when $S\{\vec{u}_h\}/S\{\vec{u}\} > 3$.
305 This suggests that our screening threshold is excessively conservative at those frequencies, and
306 that a more precise screening threshold is frequency dependent. For example, it might take into
307 account the f^3 character of the noise in $S\{\vec{u}_a\}$ (Figure A1). For the purposes of this work the
308 $S\{\vec{u}_h\}/S\{\vec{u}\} < 3$ threshold for spectral fits is sufficient, and detailed characterization of the IMU's
309 motion- and frequency-dependent noise level is left for future work.

310 *c. StableMoor Spectra*

311 The spectra of the stablemoor motion has a broader peak with a maximum amplitude that is
312 approximately half the frequency of the TTM spectral peak (Figure 9). The motion of this platform
313 also does not have high-frequency ‘sub-peaks’ or other high-frequency broad-banded excitation
314 (Part 1). These characteristics of the motion are most-likely due to the more massive and hydro-
315 dynamically streamlined properties of the platform.

316 Like the TTM, the motion-corrected spectra from the StableMoor are consistent with turbulence
317 theory and previous observations. Most importantly, there is an improvement in the quality of the
318 motion corrected spectra compared to the TTM. In particular the persistent motion contamination
319 peaks appear to be completely removed. That is, this measurement system provides an accurate
320 estimate of the turbulence spectra at this location from low frequencies to more than 1 Hz—well
321 into the inertial sub-range—for all three components of velocity.

322 Note that this level of accuracy can not be obtained without the independent estimate of \vec{u}_{low} .
323 If we assume that $\vec{u}_{low} = 0$ a similar plot to Figure 9 (not shown) reveals persistent motion-
324 contamination peaks and troughs in the u - and v -spectra regardless of the choice of f_a . This
325 indicates that the low-frequency motion of the StableMoor is below a threshold where the IMU’s
326 signal to noise ratio is high enough to resolve its motion. In other words, compared to the TTM,
327 the StableMoor platform provides a more accurate measurement of turbulence when it includes an
328 independent measure of \vec{u}_{low} (here a bottom-tracking ADCP), but it does no better—and perhaps
329 worse—when it doesn’t.

330 *d. Torpedo spectra*

331 The u and v motion of the turbulence ‘torpedo’ is broad-banded and the w motion has a narrow
332 peak at 0.3 Hz (Figure 10). Because \vec{u}_h is estimated using $f_a = 0.0333Hz$ and assuming $\vec{u}_{low} = 0$

333 its spectra rolls-off quickly below f_a . A better estimate of \vec{u}_{low} could be obtained by accounting
334 for ship motion, but this has not been done here.

335 Motion correction of the torpedo data appears to effectively remove a motion from $S\{w\}$ at
336 0.3Hz, and straightens out $S\{v\}$ between 0.04 and 0.6Hz. $S\{u\}$ is relatively unimproved by motion
337 correction, apparently because the torpedo motion is smaller than the turbulence in this direction.
338 At frequencies below f_a , $S\{u\}$ and $S\{v\}$ increase dramatically. This suggests that unresolved low-
339 frequency motion of the torpedo is contaminating the velocity measurements at these frequencies.
340 It may be possible to correct for some of this using a measurement of the ship's motion as a
341 proxy for the torpedo's low-frequency motion, but this has not been done. Still, above f_a , the
342 torpedo appears to provide a reliable estimate of spectral amplitude in the inertial subrange and
343 can therefore be used to estimate ε . Considering the simplicity of the platform it may be a useful
344 option for quantifying this essential turbulence quantity in a variety of scenarios. If a GPS is
345 positioned above it, it may be capable of providing even more.

346 *e. Cross-spectra*

347 Inspection of cross-spectra from TTM measurements demonstrates that motion correction can
348 reduce motion contamination to produce reliable estimates of velocity cross-spectra (Figure 11).
349 At low flow speeds (left column), cross-spectra between components of \vec{u}_h (i.e. between compo-
350 nents of head-motion, red) are small compared to correlated velocities. As the velocity magnitude
351 increases (center, and right columns), the swaying motion of the TTM at 0.15 Hz appears as a
352 peak in the amplitude of the cross-spectra of \vec{u}_h and \vec{u}_m (black) for all three components of cross-
353 spectra (rows). Fortunately, motion correction reduces the amplitude of this peak dramatically so
354 that $C\{\vec{u}\}$ (blue) is small at 0.15 Hz compared to lower frequencies. Furthermore, the fact that the

standard deviation of $C\{\vec{u}\}$ is also relatively small at 0.15 Hz suggests that motion correction is effective for each spectral window, not just in their mean.

These results indicate that motion-corrected TTM velocity measurements can be used to obtain reliable estimates of turbulence Reynold's stresses, which are the integral of the cross-spectra. Without motion correction, Reynold's stress estimates would be contaminated by the large peaks in the cross-spectra that are due to the swaying and fluttering motion of the TTM vane.

A similar investigation of StableMoor cross-spectra (not shown) indicates that cross-spectral motion contamination is much lower amplitude than for the TTM. The low-frequency (< 0.3 Hz) 'swimming' motion of that platform produces minimal cross-spectral signal, and the relative large-mass of the platform minimizes the kinds of higher-frequency swaying/fluttering that creates large values of cross-spectral head-motion. Thus, the StableMoor platform also produces reliable estimates of Reynold's stresses, which are presumed to be improved by motion correction.

5. Discussion

The beginning of the previous section presented a comparison of \vec{u} measured by a TTM-mounted ADV, to measurements from a co-located ADP. This demonstrated that the IMU provides a reliable estimate of the ADV's orientation and that this can be utilized to estimate mean velocity in the earth's reference frame. Turbulence velocity estimates from the same ADP are also in agreement with low-frequency TTM turbulence estimates (not shown), but the ADP does not resolve turbulence at the scales where motion contamination is strongest (0.1 to 1.0 Hz).

Ideally, moored motion-corrected turbulence velocity measurements would be validated against simultaneous independent validated measurements of turbulence velocity at the same scales, exact time and exact location. Accomplishing this, however, involves significant technical challenges not easily overcome—most notably the difficulty of measuring turbulence at the same point as

the moving ADV. A slightly less ideal but much more realistic confirmation of the methodology might involve comparing the statistics of moored turbulence measurements to that from a nearby fixed platform, or a fixed platform placed at the same location at a different time (e.g. the ‘TTT’ platform described in Thomson et al. 2012). Unfortunately, to our knowledge, these measurements have not yet been made.

Lacking a relevant, fixed, independent turbulence measurement to compare to it is instructive to demonstrate the degree to which the moored measurements are consistent with turbulence theory and other turbulence measurements in similar flow environments. The previous section showed that the shape of the turbulence velocity spectra from moored ADVs is consistent with Kolmogorov’s theory of locally isotropic turbulence, which has been observed consistently in turbulence measurements for decades (Kolmogorov 1941; Grant et al. 1962; McMillan et al. 2016). In particular, we observed an isotropic subrange—an $f^{-5/3}$ spectral slope, and equal amplitude spectra between components—that is driven by anisotropic turbulence at longer time-scales (Figures 8, 9, 10). This is interpreted as the first indication that the measurement systems presented are capable of accurately resolving turbulence. The degree to which uncorrected spectra were corrected toward this theoretical and observationally confirmed shape is interpreted as a measure of the improvement of the spectral estimates by motion correction.

Figure 12 presents a time-series of the mean velocity (A) and several turbulence statistics that were measured during the June 2014 TTM deployment. This figure shows the evolution of the flow through Admiralty Inlet during 1.5 tidal cycles. The tke (B), Reynold’s stresses (C), dissipation and one component of turbulence production (D) grow and strengthen with ebb or flood, then subside during slack tide. This component of turbulence production is:

$$P_{uz} = \frac{\partial \bar{u}}{\partial z} \overline{uw} \quad . \quad (4)$$

Where $\partial \bar{u} / \partial z$ is computed from the two ADV's on the TTM. The highest values of ε and P_{uz} occur at the peak of the ebb or flood, which is in agreement with other measurements in tidal channels. The agreement of the magnitude of P_{uz} with ε at those times suggests a local production-dissipation balance that is often observed in tidally forced channels (Trowbridge et al. 1999; Stacey et al. 1999b; McMillan et al. 2016). At other times the value of P_{uz} is insufficient to balance ε or is negative.

Inspection of the negative P_{uz} values reveals that most of them are due to a reversed sign of \overline{uw} rather than a reversed sign of $\partial u / \partial z$ (i.e. when compared to the sign of u). This suggests that uncertainty in \overline{uw} may be contributing to discrepancies between P_{uz} and ε . Furthermore, considering the complex nature of the shoreline near this site (i.e. the headland), it is unsurprising that P_{uz} does not balance ε perfectly. Other terms of the tke equation are likely to be important, such as other components of production, advection terms, or turbulent transport terms. The fact that these two terms are in near-balance as often as they are is a strong indication that bottom boundary layer physics are an important piece of the dynamics at this site.

Figure 13 compares individual values of P_{uz} with ε directly. Given the assumptions implicit in this comparison, and the discussion above, the agreement between P_{uz} and ε is an encouraging result that suggests the turbulent boundary reaches the depth of these measurements (10 m) during the highest flow speeds. This result is further supported by a comparison of \bar{U} with ε (Figure 14). Here we see a $\varepsilon \propto \bar{U}^3$ dependence that is again suggestive of bottom boundary layer physics (Trowbridge 1992; Nash et al. 2009). At lower flow speeds, ε deviates from this relationship, which suggests that the boundary layer is no longer the dominant physical process at the depth of these measurements.

6. Conclusion

This work presents a methodology for measuring turbulence from moored IMU-ADV, and details an approach for removing the IMU-measured mooring motion from the ADV’s velocity measurements. The IMU integrated into the Nortek Vector ADV has been configured to provide estimates of the ADV’s orientation and motion at every time-step of the ADV’s sampling. The tight integration of the IMU and ADV data streams provides a data set that can be used to correct velocity measurements for mooring motion and rotate those measurements into the earth’s reference frame.

Comparison of spectra of ADV head motion, $S\{\vec{u}_h\}$, to that of motion-corrected, $S\{\vec{u}\}$, and uncorrected spectra, $S\{\vec{u}_m\}$, reveals that motion correction improves spectral estimates of moored ADV measurements. In particular, we find motion corrected spectra have spectral shapes that are similar to previous measurements of tidal-channel turbulence and have a $f^{-5/3}$ spectral slope at high frequencies. This suggests that the motion-corrected spectra resolve the inertial subrange predicted by Kolmogorov’s theory of locally isotropic turbulence.

Motion correction reduces motion contamination for all platforms we presented, but it does not necessarily remove it completely. This seems to depend on the relative amplitude of platform motion compared to the underlying turbulence being measured. The most notable example of this is from the TTM, which has a large ‘swaying’ peak at 0.1 Hz. Where this peak is very large—especially in the v -component—it is not reduced to a level that is consistent with earlier measurements of tidal-channel turbulence—i.e. there is no ‘smooth roll-off’ between low-frequency energy-containing scales and the $f^{-5/3}$ inertial subrange.

This inconsistency indicates that turbulence measurements from moored, motion-corrected IMU-ADV must be interpreted with care. An inspection of spectra presented here suggests

445 that excluding spectral regions where $S\{\vec{u}_h\}/S\{\vec{u}\} > 3$ removes ‘persistent motion contamina-
446 tion’ peaks, while still preserving spectral regions where motion correction is effective. Using this
447 criteria it is then possible to produce spectral fits that exclude persistent motion contamination,
448 and provide reliable estimates of turbulence quantities of interest (e.g. ε and τ_{ke}).

449 We also find that motion correction reduces motion contamination in cross-spectra. This is im-
450 portant because it suggests that moored IMU-ADV measurements may be used to produce reliable
451 estimates of Reynolds stresses. We utilized these stress estimates and vertical shear estimates,
452 both from the TTM, to estimate P_{uz} .

453 Finally, we’ve shown that ε estimates based on motion-corrected spectra scale with the U^3 , and
454 balance P_{uz} estimates during ebb and flood. Together, these results indicate that bottom boundary
455 layer physics are a dominant process at this site, and that the boundary layer reaches the height of
456 the IMU-ADVs (10 m) during ebb and flood. The degree of agreement between P_{uz} and ε also
457 serves as an indicator of the self-consistency of moored IMU-ADV turbulence measurements.

458 *Acknowledgments.* Many thanks to Joe Talbert, Alex DeKlerk, Captain Andy Reay-Ellers, Jen-
459 nifer Rinker, Maricarmen Guerra, and Eric Nelson in assisting with data collection. The authors
460 are also grateful to James VanZwieten, Matthew Egeland and Marshall Richmond for discussion
461 on the details of this work.

A1. Comparing StableMoor \vec{u}_{low} to IMU \vec{u}_{h}

In order to better understand the IMU's signal-to-noise ratio, it is instructive to compare the motion of the StableMoor buoy from the ADP bottom track measurements, u_{BT} , to the IMU's estimates of ADP motion. To do this, we compute the IMU's estimate of ADP motion using equation (2), and replacing ℓ^* with the vector that points from the IMU to the ADP head. We then linearly interpolated the ADP measurements onto the times of the ADV-IMU measurements.

The coherence between these two signals is high and statistically significant over 1.5 decades (from 0.03 to 0.8 Hz). The v component has the highest coherence, 98%, because this is the direction that has the most motion and therefore these estimates have a higher signal to noise ratio. The u and w components have slightly lower coherence, 80% and 65%, respectively, which indicates the *convolved* signal to noise ratio of these measurements.

On the low-frequency side, our interpretation is that the signal to noise ratio of the IMU increases dramatically below 0.03 Hz, resulting in low coherence. On the high-frequency side Doppler-noise in the ADP measurements contaminates its estimates of motion, causing the decrease in coherence at 0.8 Hz. A comparison of the phase between these signals shows that there is no lag between the measurements (not shown).

These results help to inform the selection of zero-lag filters used to estimate \vec{u}_{low} from u_{BT} . In particular, by selecting 0.2 Hz, we target the middle of the coherence peak between the two measurements. Furthermore, the rapid decrease in coherence below 0.03 Hz provides an objective measure of the performance of the frequency at which IMU measured velocity becomes unreliable in the flow conditions we observed.

References

- Afgan, I., J. McNaughton, S. Rolfo, D. Apsley, T. Stallard, and P. Stansby, 2013: Turbulent flow and loading on a tidal stream turbine by les and rans. *International Journal of Heat and Fluid Flow*, **43**, 96–108.
- Alexander, S. R., and P. E. Hamlington, 2015: Analysis of turbulent bending moments in tidal current boundary layers. *Journal of Renewable and Sustainable Energy*, **7** (6), 063 118.
- Alford, M. H., 2010: Sustained, full-water-column observations of internal waves and mixing near mendocino escarpment. *Journal of Physical Oceanography*, **40** (12), 2643–2660, doi: 10.1175/2010JPO4502.1, URL <http://dx.doi.org/10.1175/2010JPO4502.1>, <http://dx.doi.org/10.1175/2010JPO4502.1>.
- Bachmann, E. R., X. Yun, D. McKinney, R. B. McGhee, and M. J. Zyda, 2003: Design and implementation of MARG sensors for 3-DOF orientation measurement of rigid bodies. *International Conference on Robotics & Automation*, Taipei, Taiwan.
- Barshan, B., and H. F. Durrant-Whyte, 1995: Inertial navigation systems for mobile robots. *IEEE Transactions on Robotics and Automation*, **11** (3), 328–342.
- Bevly, D. M., 2004: Global positioning system (gps): A low-cost velocity sensor for correcting inertial sensor errors on ground vehicles. *Journal of dynamic systems, measurement, and control*, **126** (2), 255–264.
- Cartwright, G. M., C. T. Friedrichs, P. J. Dickhudt, T. Gass, and F. H. Farmer, 2009: Using the acoustic doppler velocimeter (adv) in the mudbed real-time observing system. *Marine Technology for Our Future: Global and Local Challenges*.

505 Doherty, K., D. Frye, S. Liberatore, and J. Toole, 1999: A moored profiling instrument*. *Journal*
506 *of Atmospheric and Oceanic Technology*, **16** (11), 1816–1829.

507 Egeland, M. N., 2014: Spectral evaluation of motion compensated ADV systems for ocean turbu-
508 lence measurements. Ph.D. thesis, Florida Atlantic University.

509 Fer, I., and M. B. Paskyabi, 2014: Autonomous ocean turbulence measurements using shear probes
510 on a moored instrument. *Journal of Atmospheric and Oceanic Technology*, **31** (2), 474–490, doi:
511 10.1175/JTECH-D-13-00096.1, URL <http://dx.doi.org/10.1175/JTECH-D-13-00096.1>, [http://](http://dx.doi.org/10.1175/JTECH-D-13-00096.1)
512 dx.doi.org/10.1175/JTECH-D-13-00096.1.

513 Finlayson, D., 2005: Combined bathymetry and topography of the Puget Lowlands, Washington
514 state. URL <http://www.ocean.washington.edu/data/pugetsound/>.

515 Geyer, R. W., M. E. Scully, and D. K. Ralston, 2008: Quantifying vertical mixing in estuaries.
516 *Environmental Fluid Mechanics*, **8**, 495–509, doi:10.1007/s10652-008-9107-2.

517 Goodman, L., E. R. Levine, and R. G. Lueck, 2006: On measuring the terms of the turbulent
518 kinetic energy budget from an auv. *Journal of Atmospheric and Oceanic Technology*, **23** (7),
519 977–990, doi:10.1175/JTECH1889.1, URL <http://dx.doi.org/10.1175/JTECH1889.1>, [http://dx.](http://dx.doi.org/10.1175/JTECH1889.1)
520 [doi.org/10.1175/JTECH1889.1](http://dx.doi.org/10.1175/JTECH1889.1).

521 Grant, H. L., R. W. Stewart, and A. Moilliet, 1962: Turbulence spectra from a tidal channel.
522 *Journal of Fluid Mechanics*, **12**, 241–263.

523 Gulmammadov, F., 2009: Analysis, modeling and compensation of bias drift in mems inertial
524 sensors. *Recent Advances in Space Technologies, 2009. RAST'09. 4th International Conference*
525 *on*, IEEE, 591–596.

Gunawan, B., V. S. Neary, and J. Colby, 2014: Tidal energy site resource assessment in the East River tidal strait, near Roosevelt Island, New York, NY (USA). *Renewable Energy*, **71**, 509–517, doi:10.1016/j.renene.2014.06.002.

Hand, M. M., N. D. Kelley, and M. J. Balas, 2003: Identification of wind turbine response to turbulent inflow structures. Tech. Rep. NREL/CP-500-33465, National Renewable Energy Laboratory.

Harding, S., L. Kilcher, and J. Thomson, 2017: Turbulence measurements from compliant moorings - part 1: Motion characterization, in review.

Kelley, N. D., B. J. Jonkman, G. N. Scott, J. T. Bialasiewicz, and L. S. Redmond, 2005: The impact of coherent turbulence on wind turbine aeroelastic response and its simulation. *WindPower*, Denver, Colorado, NREL/CP-500-38074, may 15-18.

Kilcher, L., J. Thomson, J. Talbert, and A. DeKlerk, 2016: Measuring turbulence from moored acoustic Doppler velocimeters: A manual to quantifying inflow at tidal energy sites. Tech. Rep. 62979, National Renewable Energy Laboratory. URL www.nrel.gov/docs/fy16osti/62979.pdf.

Kim, S. C., C. T. Friedrichs, J. P.-Y. Maa, and L. D. Wright, 2000: Estimating bottom stress in tidal boundary layer from acoustic doppler velocimeter data. *Journal of Hydraulic Engineering*, 399–406.

Kolmogorov, A. N., 1941: Dissipation of energy in the locally isotropic turbulence. *Dokl. Akad. Nauk SSSR*, **32** (1), 16–18, URL <http://www.jstor.org/stable/51981>.

Kraus, C., A. Lohrmann, and R. Cabrera, 1994: A new acoustic meter for measuring 3d laboratory flows. *Journal of Hydraulic Engineering*, **120**, 406–412.

547 Lohrmann, A., R. Cabrera, G. Gelfenbaum, and J. Haines, 1995: Direct measurements of reynolds
548 stress with an acoustic doppler velocimeter. *Current Measurement, 1995., Proceedings of the*
549 *IEEE Fifth Working Conference on*, 205–210, doi:10.1109/CCM.1995.516175.

550 Lorke, A., 2007: Boundary mixing in the thermocline of a large lake. *Journal of Geophysical*
551 *Research: Oceans*, **112 (C9)**, n/a–n/a, doi:10.1029/2006JC004008, URL [http://dx.doi.org/10.](http://dx.doi.org/10.1029/2006JC004008)
552 [1029/2006JC004008](http://dx.doi.org/10.1029/2006JC004008), c09019.

553 Lueck, R. G., and D. Huang, 1999: Dissipation measurement with a moored instrument in a swift
554 tidal channel. *Journal of atmospheric and oceanic technology*, **16**, 1499–1505.

555 Lumley, J., and E. Terray, 1983: Kinematics of turbulence convected by a random wave field.
556 *Journal of Physical Oceanography*, **13 (11)**, 2000–2007.

557 McCaffrey, K., B. Fox-Kemper, P. E. Hamlington, and J. Thomson, 2015: Characterization of
558 turbulence anisotropy, coherence, and intermittency at a prospective tidal energy site: Observa-
559 tional data analysis. *Renewable Energy*, **76**, 441–453.

560 McMillan, J. M., A. E. Hay, R. G. Lueck, and F. Wolk, 2016: Rates of dissipation of turbulent ki-
561 netic energy in a high reynolds number tidal channel. *Journal of Atmospheric and Oceanic Tech-*
562 *nology*, **33 (4)**, 817–837, doi:10.1175/JTECH-D-15-0167.1, URL [http://dx.doi.org/10.1175/](http://dx.doi.org/10.1175/JTECH-D-15-0167.1)
563 [JTECH-D-15-0167.1](http://dx.doi.org/10.1175/JTECH-D-15-0167.1), <http://dx.doi.org/10.1175/JTECH-D-15-0167.1>.

564 MicroStrain, I., 2010: Technical note: Coning and sculling. Tech. Rep. I0019, MicroStrain. URL
565 http://files.microstrain.com/TN-I0019_3DM-GX3-25__Coning_And_Sculling.pdf.

566 MicroStrain, I., 2012: *3DM-GX3-15,-25 MIP Data Communications Protocol*. URL [http:](http://files.microstrain.com/3DM-GX3-15-25-MIP-Data-Communications-Protocol.pdf)
567 [//files.microstrain.com/3DM-GX3-15-25-MIP-Data-Communications-Protocol.pdf](http://files.microstrain.com/3DM-GX3-15-25-MIP-Data-Communications-Protocol.pdf), retrieved
568 January 2014.

569 Miller, S. D., T. S. Hristov, J. B. Edson, and C. A. Friehe, 2008: Platform motion effects on
570 measurements of turbulence and air-sea exchange over the open ocean. *Journal of Atmospheric*
571 *and Oceanic Technology*, **25** (9), 1683–1694, doi:10.1175/2008JTECHO547.1, URL [http://dx.](http://dx.doi.org/10.1175/2008JTECHO547.1)
572 [doi.org/10.1175/2008JTECHO547.1](http://dx.doi.org/10.1175/2008JTECHO547.1), <http://dx.doi.org/10.1175/2008JTECHO547.1>.

573 Morison, J. R., J. W. Johnson, and S. A. Schaaf, 1950: The force exerted by surface waves on
574 piles. *Journal of Petroleum Technology*, **2** (05), 149–154.

575 Moum, J., and J. Nash, 2009: Mixing measurements on an equatorial ocean mooring. *Journal of*
576 *Atmospheric and Oceanic Technology*, **26** (2), 317–336.

577 Mücke, T., D. Kleinhans, and J. Peinke, 2011: Atmospheric turbulence and its influence on the
578 alternating loads on wind turbines. *Wind Energy*, **14**, 301–316.

579 Nash, J. D., L. F. Kilcher, and J. N. Moum, 2009: Structure and composition of a strongly
580 stratified, tidally pulsed river plume. *Journal of Geophysical Research*, **114**, C00B12, doi:
581 [10.1029/2008JC005036](https://doi.org/10.1029/2008JC005036).

582 Nash, J. D., E. Kunze, J. M. Toole, and R. W. Schmitt, 2004: Internal tide reflec-
583 tion and turbulent mixing on the continental slope. *Journal of Physical Oceanography*,
584 **34** (5), 1117–1134, doi:10.1175/1520-0485(2004)034<1117:ITRATM>2.0.CO;2, URL [http://](http://dx.doi.org/10.1175/1520-0485(2004)034<1117:ITRATM>2.0.CO;2)
585 [dx.doi.org/10.1175/1520-0485\(2004\)034<1117:ITRATM>2.0.CO;2](http://dx.doi.org/10.1175/1520-0485(2004)034<1117:ITRATM>2.0.CO;2), [http://dx.doi.org/10.1175/](http://dx.doi.org/10.1175/1520-0485(2004)034<1117:ITRATM>2.0.CO;2)
586 [1520-0485\(2004\)034<1117:ITRATM>2.0.CO;2](http://dx.doi.org/10.1175/1520-0485(2004)034<1117:ITRATM>2.0.CO;2).

587 Nortek, 2005: *Vector Current Meter User Manual*. Vangkroken 2, NO-1351 RUD, Norway, h ed.

588 oáo Luis Marins, J., X. Yun, E. R. Bachmann, R. B. McGhee, and M. J. Zyda, 2001: An extended
589 Kalman filter for quaternion-based orientation estimation using MARG sensors. *Internation*
590 *conference on intelligent robots and systems*.

591 Paskyabi, M. B., and I. Fer, 2013: Turbulence measurements in shallow water from
 592 a subsurface moored moving platform. *Energy Procedia*, **35**, 307 – 316, doi:http://dx.
 593 doi.org/10.1016/j.egypro.2013.07.183, URL [http://www.sciencedirect.com/science/article/pii/](http://www.sciencedirect.com/science/article/pii/S1876610213012691)
 594 S1876610213012691.

595 Rippeth, T. P., E. Williams, and J. H. Simpson, 2002: Reynolds stress and turbulent en-
 596 ergy production in a tidal channel. *Journal of Physical Oceanography*, **32**, 1242–1251, doi:
 597 10.1175/1520-0485(2002)032\$(<\$1242:RSATEP\$>\$2.0.CO;2.

598 Sreenivasan, K. R., 1995: On the universality of the Kolmogorov constant. *Physics of Fluids*, **7**,
 599 2778–2784.

600 Stacey, M. T., S. G. Monismith, and J. R. Burau, 1999a: Measurements of reynolds stress profiles
 601 in unstratified tidal flow. *J. Geophys. Res.*, **104 (C5)**, 10 933–10 949, URL [http://dx.doi.org/10.](http://dx.doi.org/10.1029/1998JC900095)
 602 1029/1998JC900095.

603 Stacey, M. T., S. G. Monismith, and J. R. Burau, 1999b: Observations of turbulence in a partially
 604 stratified estuary. *Journal of Physical Oceanography*, **29**, 1950–1970.

605 Thomson, J., B. Polagye, V. Durgesh, and M. Richmond, 2012: Measurements of turbulence at
 606 two tidal energy sites in Puget Sound, WA. *Journal of Oceanic Engineering*, **37 (3)**, 363–374,
 607 doi:10.1109/JOE.2012.2191656.

608 Trowbridge, J. H., 1992: A simple description of the deepening and structure of a stably stratified
 609 flow driven by a surface stress. *Journal of Geophysical Research*, **97**, 15 529–15 543.

610 Trowbridge, J. H., W. R. Geyer, M. M. Bowen, and A. J. I. Williams, 1999: Near-bottom turbu-
 611 lence measurements in a partially mixed estuary: turbulent energy balance, velocity structure
 612 and along-channel momentum balance. *Journal of Physical Oceanography*, **29**, 3056–3072.

613 van der Walt, S., S. C. Colbert, and G. Varoquaux, 2011: The numpy array: A structure for efficient
614 numerical computation. *Computing in Science & Engineering*, **13**, 22–30, doi:10.1109/MCSE.
615 2011.37, URL <http://scitation.aip.org/content/aip/journal/cise/13/2/10.1109/MCSE.2011.37>.

616 VanZwieten, J. H., M. N. Egeland, K. D. von Ellenrieder, J. W. Lovenbury, and L. Kilcher, 2015:
617 Experimental evaluation of motion compensated adv measurements for in-stream hydrokinetic
618 applications. *Current, Waves and Turbulence Measurement (CWTM), 2015 IEEE/OES Eleventh*,
619 1–8, doi:10.1109/CWTM.2015.7098119.

620 Voulgaris, G., and J. H. Trowbridge, 1998: Evaluation of the acoustic doppler velocimeter (adv)
621 for turbulence measurements. *Journal of Atmospheric and Oceanic technology*, **15**, 272–289.

622 Walter, R. K., N. J. Nidzieko, and S. G. Monismith, 2011: Similarity scaling of turbulence spectra
623 and cospectra in a shallow tidal flow. *Journal of Geophysical Research: Oceans*, **116** (C10).

624 Wiles, P. J., T. P. Rippeth, J. H. Simpson, and P. J. Hendricks, 2006: A novel technique for
625 measuring the rate of turbulent dissipation in the marine environment. *Geophysical Research*
626 *Letters*, **33**, 21 608.

627 Winkel, D., M. Gregg, and T. Sanford, 1996: Resolving oceanic shear and velocity with the multi-
628 scale profiler. *Journal of Atmospheric and Oceanic Technology*, **13** (5), 1046–1072.

629 Wyngaard, J. C., L. Rockwell, and C. A. Friehe, 1985: Errors in the measurement of turbulence
630 upstream of an axisymmetric body. *Journal of Atmospheric and Oceanic Technology*, **2** (4),
631 605–614.

632 Zhang, Y., K. Streitlien, J. G. Bellingham, and A. B. Baggeroer, 2001: Acoustic
633 doppler velocimeter flow measurement from an autonomous underwater vehicle with
634 applications to deep ocean convection. *Journal of Atmospheric and Oceanic Tech-*

635 *nology*, **18** (12), 2038–2051, doi:10.1175/1520-0426(2001)018<2038:ADVFMF>2.0.CO;2,
636 URL [http://dx.doi.org/10.1175/1520-0426\(2001\)018<2038:ADVFMF>2.0.CO;2](http://dx.doi.org/10.1175/1520-0426(2001)018<2038:ADVFMF>2.0.CO;2), [http://dx.doi.](http://dx.doi.org/10.1175/1520-0426(2001)018<2038:ADVFMF>2.0.CO;2)
637 [org/10.1175/1520-0426\(2001\)018<2038:ADVFMF>2.0.CO;2](http://dx.doi.org/10.1175/1520-0426(2001)018<2038:ADVFMF>2.0.CO;2).

LIST OF FIGURES

638			
639	Fig. 1.	Bathymetry of Admiralty Inlet near Port Townsend, Washington, U.S.A. (Finlayson 2005). The red dot indicates the location of all measurements. The positive u direction is the direction of ebb flow (thick arrow originating from red dot), and positive v is away from Admiralty Head (smaller arrow).	34
640			
641			
642			
643	Fig. 2.	Schematic diagram of the TTM, not to scale.	35
644	Fig. 3.	TTM components on the deck of the R/V Jack Robertson. The TTM includes two ADVs, with pressure-cases mounted on opposite sides of the fin. The anchor stack includes a pop-up buoy for retrieval. The green arrow indicates the vector from the IMU to the ADV head (face of the transmit transducer).	36
645			
646			
647			
648	Fig. 4.	Top: Alex DeKlerk checks to ensure that the StableMoor buoy is properly fastened to its anchor; the RDI workhorse ADCP can be seen in the rear instrument bay. A bridle is draped across the top of the buoy for deployment and recovery, and a small marker buoy fastened to the tail is useful during recovery. Bottom: a close-up of the StableMoor in the ‘nose mode’ configuration shows the ADV head and the top of its pressure case. The green arrow indicates the vector from the IMU to the ADV head.	37
649			
650			
651			
652			
653			
654	Fig. 5.	The turbulence platform showing details of the ADV head and pressure case configuration. The green arrow indicates the vector from the IMU to the ADV head. The head-cable was taped out of the way beneath the sounding weight tail fins shortly after taking this photo.	38
655			
656			
657	Fig. 6.	Spectra of \vec{u}_ω (yellow) and \vec{u}_a signals from the Microstrain IMU sitting on a motionless table. The \vec{u}_a signals are unfiltered (black), and high-pass filtered at 30s (magenta), 10s (blue), 5s (green). Vertical dotted lines indicate the filter frequency. The black horizontal dotted line indicates the noise-level of a Nortek Vector ADV configured to measure $\pm 4\text{m/s}$. The shaded region indicates the range of spectra presented herein ($0.002 < \text{tke} < 0.03 \text{ m}^2/\text{s}^2$, $1\text{e-}5 < \varepsilon < 5\text{e-}4 \text{ W/kg}$).	39
658			
659			
660			
661			
662			
663	Fig. 7.	Time series of tidal velocity at Admiralty Head from TTM measurements (black), and an acoustic Doppler profiler (red). The profiler measurements—taken at the same depth as the ADV on the TTM—were contaminated by acoustic reflection from the strongback fin when it was inline with one of the profiler’s beams. Note that the vertical scale on the three axes vary by more than an order of magnitude; the small ticks in A and B are equivalent to the ticks in C.	40
664			
665			
666			
667			
668			
669	Fig. 8.	Turbulence spectra from the June 2014 TTM deployment. Each column is for a range of streamwise velocity magnitudes (indicated at top). The rows are for each component of velocity (indicated to the lower-right of the right column). The uncorrected spectra are in black and the corrected spectra are blue, and the spectra of ADV head motion, \vec{u}_h , is red (also indicated in the legend). The vertical red dotted line indicates the filter frequency applied to the IMU accelerometers when estimating \vec{u}_h ; below this frequency $S\{\vec{u}_h\}$ is plotted as a dashed line. Diagonal black dotted lines indicate a $f^{-5/3}$ slope. The number of spectral-ensembles, N , in each column is indicated in the top row.	41
670			
671			
672			
673			
674			
675			
676			
677	Fig. 9.	Turbulence spectra from the StableMoor buoy. The axes-layout and annotations are identical to Figure 8, except that $S\{\vec{u}_h\}$ is plotted as a solid line at all frequencies because it is measured at all frequencies.	42
678			
679			

680	Fig. 10.	Turbulence spectra from the turbulence torpedo during a 35 minute period when the mean velocity was 1.3 m/s. Annotations and line colors are identical to Figure 8.	43
681			
682	Fig. 11.	The real part of the cross-spectral density between velocity components measured by the TTM. The upper-row is the u - v cross-spectral density, the middle-row is the u - w cross-spectral density, and the bottom-row is the v - w cross-spectral density. The columns are for different ranges of the stream-wise mean velocity magnitude (indicated above the top row). The blue line is the cross-spectrum between components of motion-corrected velocity, the red line is the cross-spectrum between components of head-motion, and the black line is the cross-spectrum between components of uncorrected velocity. The light-blue shading indicates one standard deviation of the C for the motion corrected cross-spectral density. N is the number of spectral ensembles in each column. The number in the lower right corner of each panel is the motion-corrected Reynold's stress (integral of the blue line) in units of $1\text{e-}4 \text{ m}^2\text{s}^{-2}$	44
683			
684			
685			
686			
687			
688			
689			
690			
691			
692			
693	Fig. 12.	Time-series of mean velocities (A), turbulence energy and its components (B), Reynold's stresses (C), and turbulence dissipation rate (D) measured by the TTM during the June, 2014 deployment. Shading indicates periods of ebb ($\bar{u} > 1.0$, grey), and flood ($\bar{u} < -1.0$, lighter grey).	45
694			
695			
696			
697	Fig. 13.	$P_{u\bar{z}}$ vs. ε during the June 2014 TTM deployment for values of $ u > 1$ m/s. Values of 'negative' production are indicated as open circles.	46
698			
699	Fig. 14.	A log-log plot of ε versus \bar{U} for the June 2014 TTM (diamonds) and May 2015 StableMoor (dots) deployments, during ebb (left) and flood (right). Black points are 5 minute averages. Green dots are mean values within speed bins of 0.2 m s^{-1} width that have at least 10 points (50 minutes of data); their vertical bars are 95% bootstrap confidence intervals. The blue line shows a U^3 slope, where the proportionality constant (blue box) is calculated by taking the log-space mean of ε/U^3	47
700			
701			
702			
703			
704			
705	Fig. 15.	Coherence between IMU-measured motion of StableMoor buoy and ADP bottom track velocity for $1.0 < \bar{U} < 1.5$. The vertical dotted line indicates the 95% confidence level for the 102 spectral windows in this estimate.	48
706			
707			

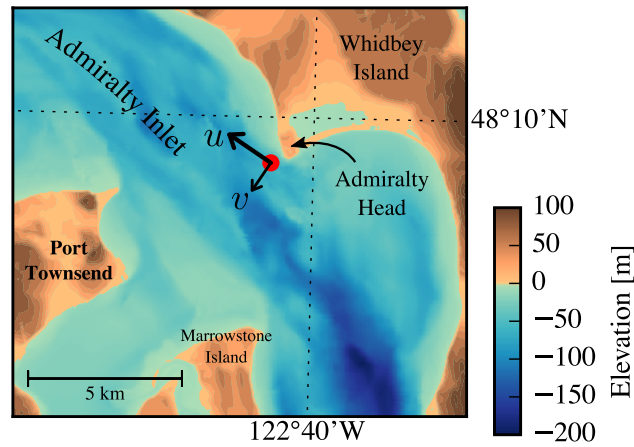


FIG. 1. Bathymetry of Admiralty Inlet near Port Townsend, Washington, U.S.A. (Finlayson 2005). The red dot indicates the location of all measurements. The positive u direction is the direction of ebb flow (thick arrow originating from red dot), and positive v is away from Admiralty Head (smaller arrow).

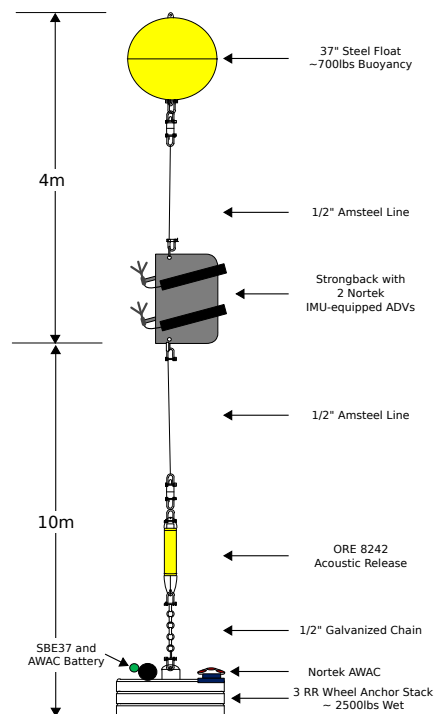
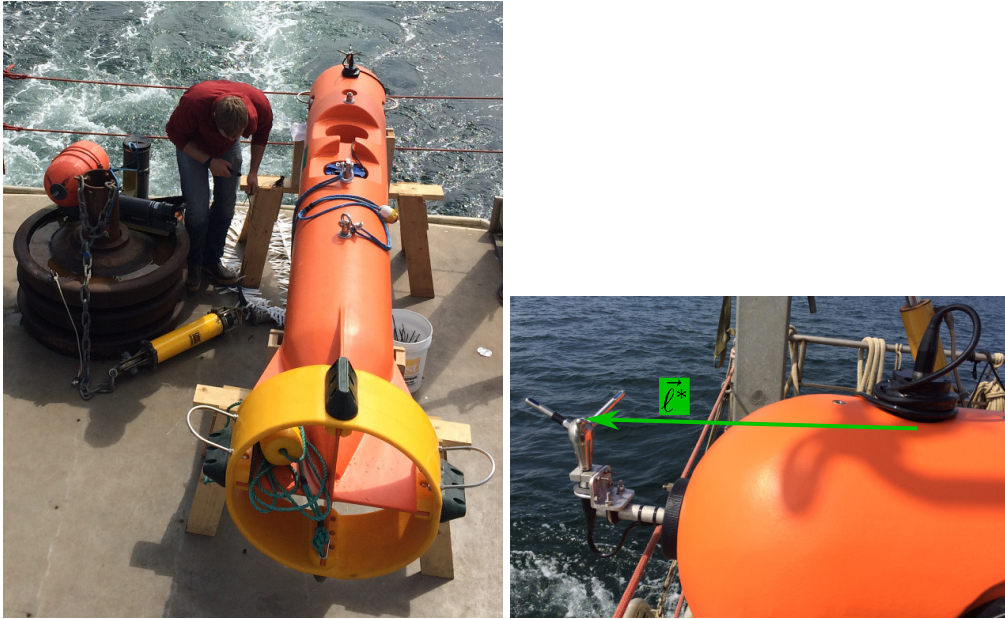


FIG. 2. Schematic diagram of the TTM, not to scale.



711 FIG. 3. TTM components on the deck of the R/V Jack Robertson. The TTM includes two ADVs, with
 712 pressure-cases mounted on opposite sides of the fin. The anchor stack includes a pop-up buoy for retrieval. The
 713 green arrow indicates the vector from the IMU to the ADV head (face of the transmit transducer).



714 FIG. 4. Top: Alex DeKlerk checks to ensure that the StableMoor buoy is properly fastened to its anchor; the
 715 RDI workhorse ADCP can be seen in the rear instrument bay. A bridle is draped across the top of the buoy
 716 for deployment and recovery, and a small marker buoy fastened to the tail is useful during recovery. Bottom: a
 717 close-up of the StableMoor in the ‘nose mode’ configuration shows the ADV head and the top of its pressure
 718 case. The green arrow indicates the vector from the IMU to the ADV head.



719 FIG. 5. The turbulence platform showing details of the ADV head and pressure case configuration. The green
720 arrow indicates the vector from the IMU to the ADV head. The head-cable was taped out of the way beneath the
721 sounding weight tail fins shortly after taking this photo.

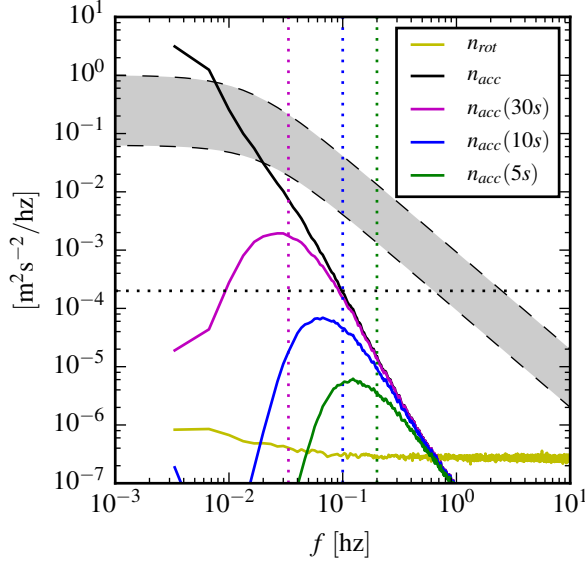
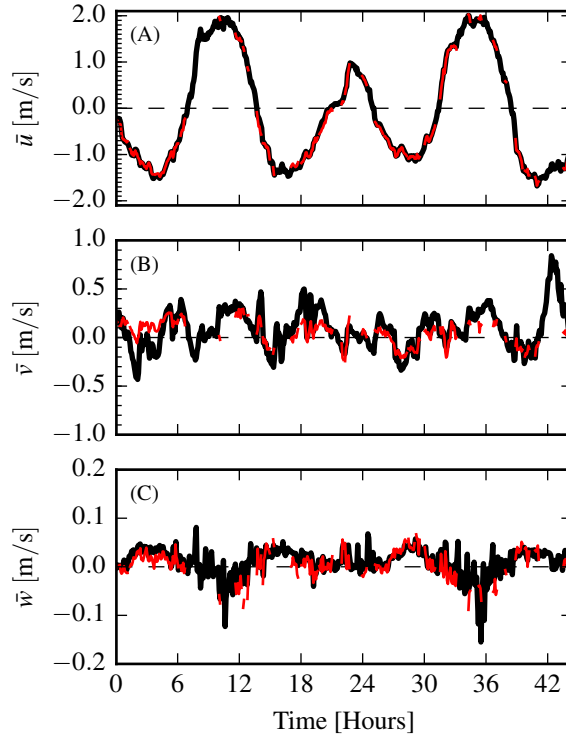


FIG. 6. Spectra of \vec{u}_ω (yellow) and \vec{u}_a signals from the Microstrain IMU sitting on a motionless table. The \vec{u}_a signals are unfiltered (black), and high-pass filtered at 30s (magenta), 10s (blue), 5s (green). Vertical dotted lines indicate the filter frequency. The black horizontal dotted line indicates the noise-level of a Nortek Vector ADV configured to measure $\pm 4\text{m/s}$. The shaded region indicates the range of spectra presented herein ($0.002 < \text{tke} < 0.03 \text{ m}^2/\text{s}^2$, $1\text{e-}5 < \varepsilon < 5\text{e-}4 \text{ W/kg}$).



727 FIG. 7. Time series of tidal velocity at Admiralty Head from TTM measurements (black), and an acoustic
 728 Doppler profiler (red). The profiler measurements—taken at the same depth as the ADV on the TTM—were
 729 contaminated by acoustic reflection from the strongback fin when it was inline with one of the profiler’s beams.
 730 Note that the vertical scale on the three axes vary by more than an order of magnitude; the small ticks in A and
 731 B are equivalent to the ticks in C.

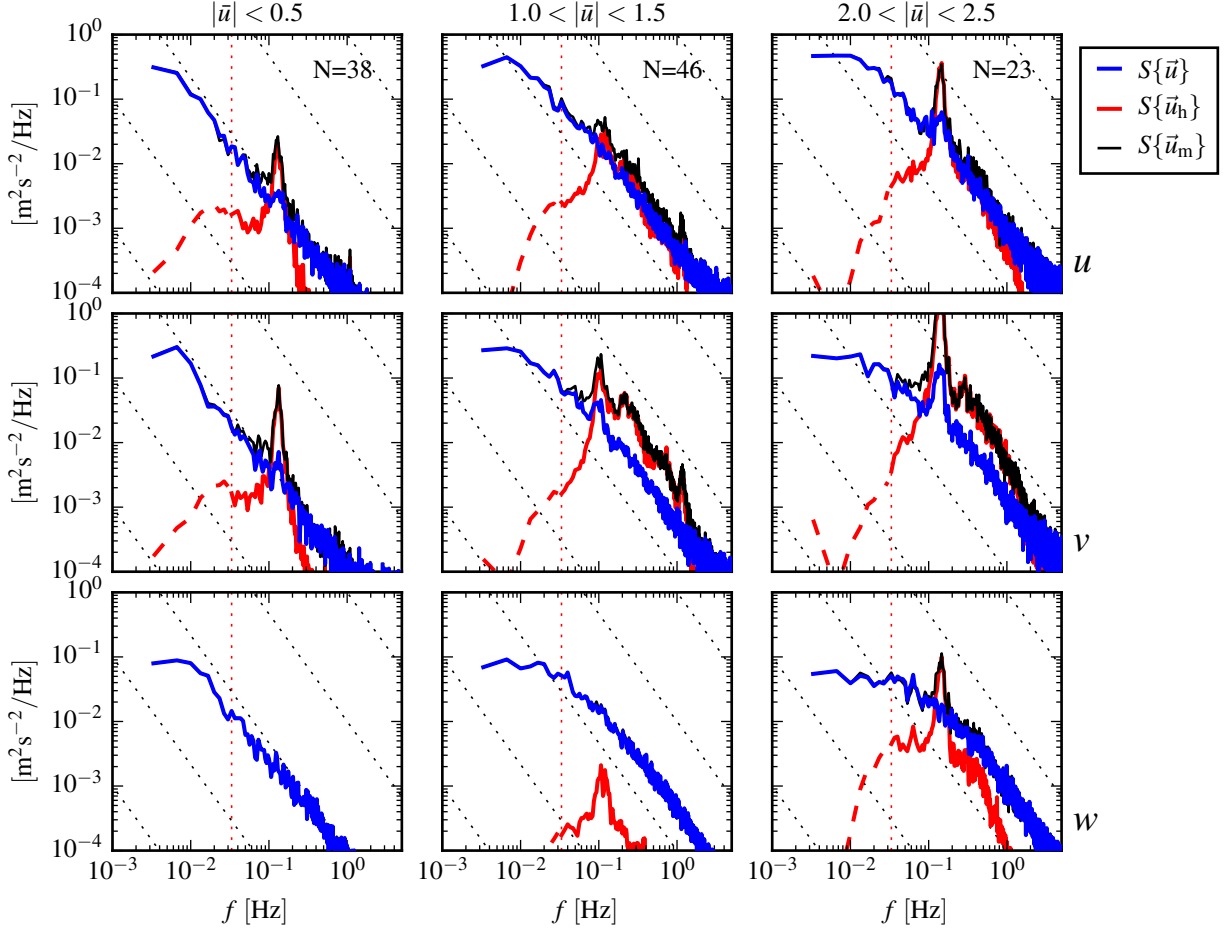


FIG. 8. Turbulence spectra from the June 2014 TTM deployment. Each column is for a range of streamwise velocity magnitudes (indicated at top). The rows are for each component of velocity (indicated to the lower-right of the right column). The uncorrected spectra are in black and the corrected spectra are blue, and the spectra of ADV head motion, \vec{u}_h , is red (also indicated in the legend). The vertical red dotted line indicates the filter frequency applied to the IMU accelerometers when estimating \vec{u}_h ; below this frequency $S\{\vec{u}_h\}$ is plotted as a dashed line. Diagonal black dotted lines indicate a $f^{-5/3}$ slope. The number of spectral-ensembles, N , in each column is indicated in the top row.

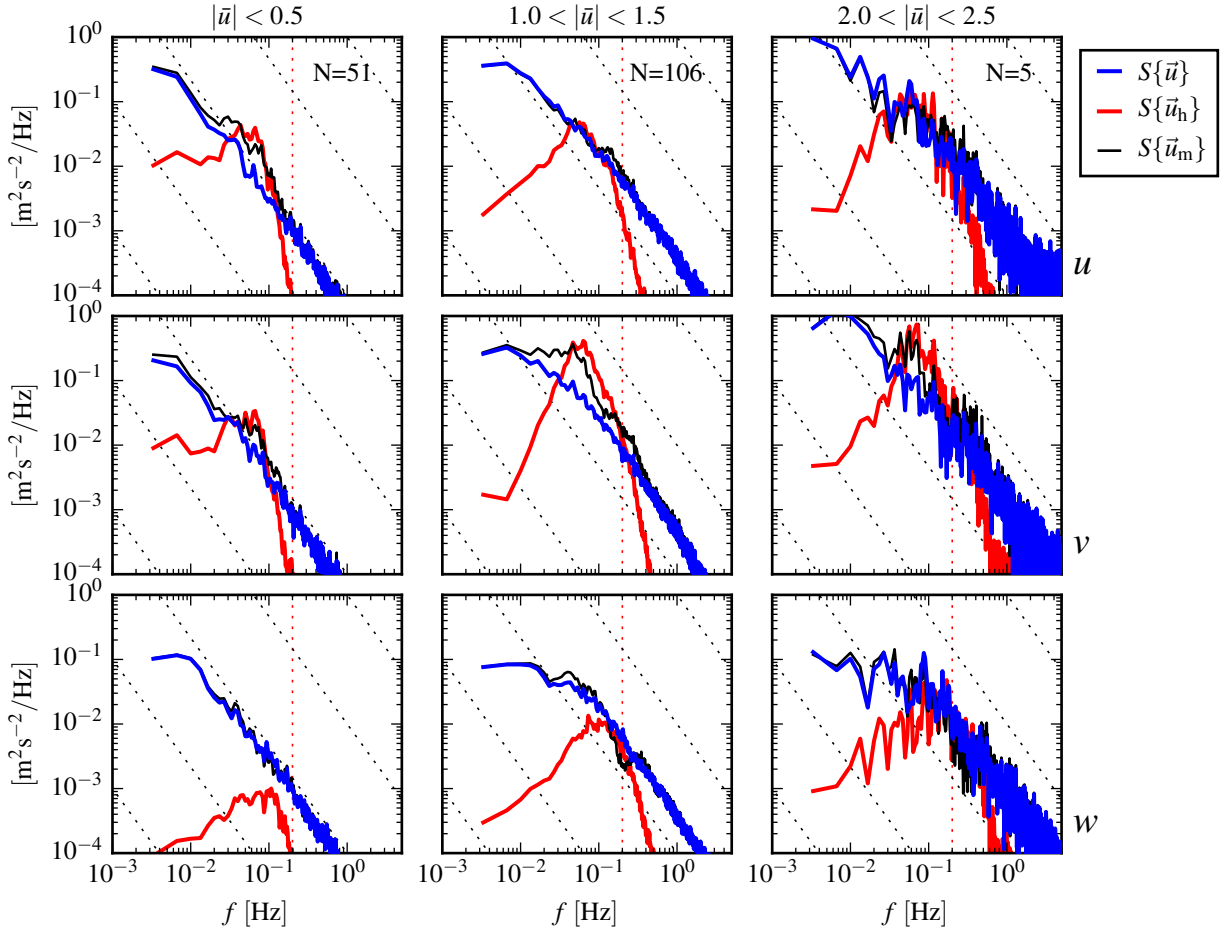


FIG. 9. Turbulence spectra from the StableMoor buoy. The axes-layout and annotations are identical to Figure 8, except that $S\{\vec{u}_h\}$ is plotted as a solid line at all frequencies because it is measured at all frequencies.

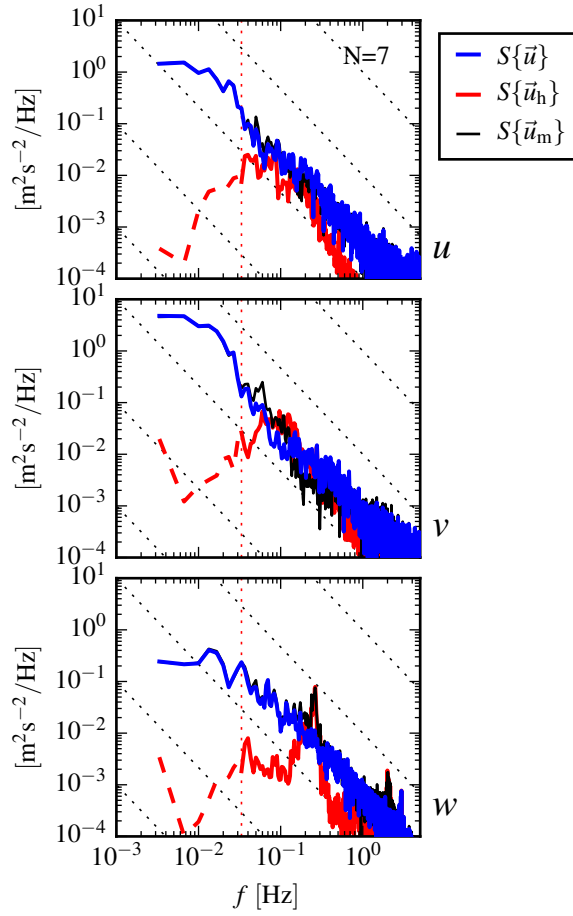


FIG. 10. Turbulence spectra from the turbulence torpedo during a 35 minute period when the mean velocity was 1.3 m/s. Annotations and line colors are identical to Figure 8.

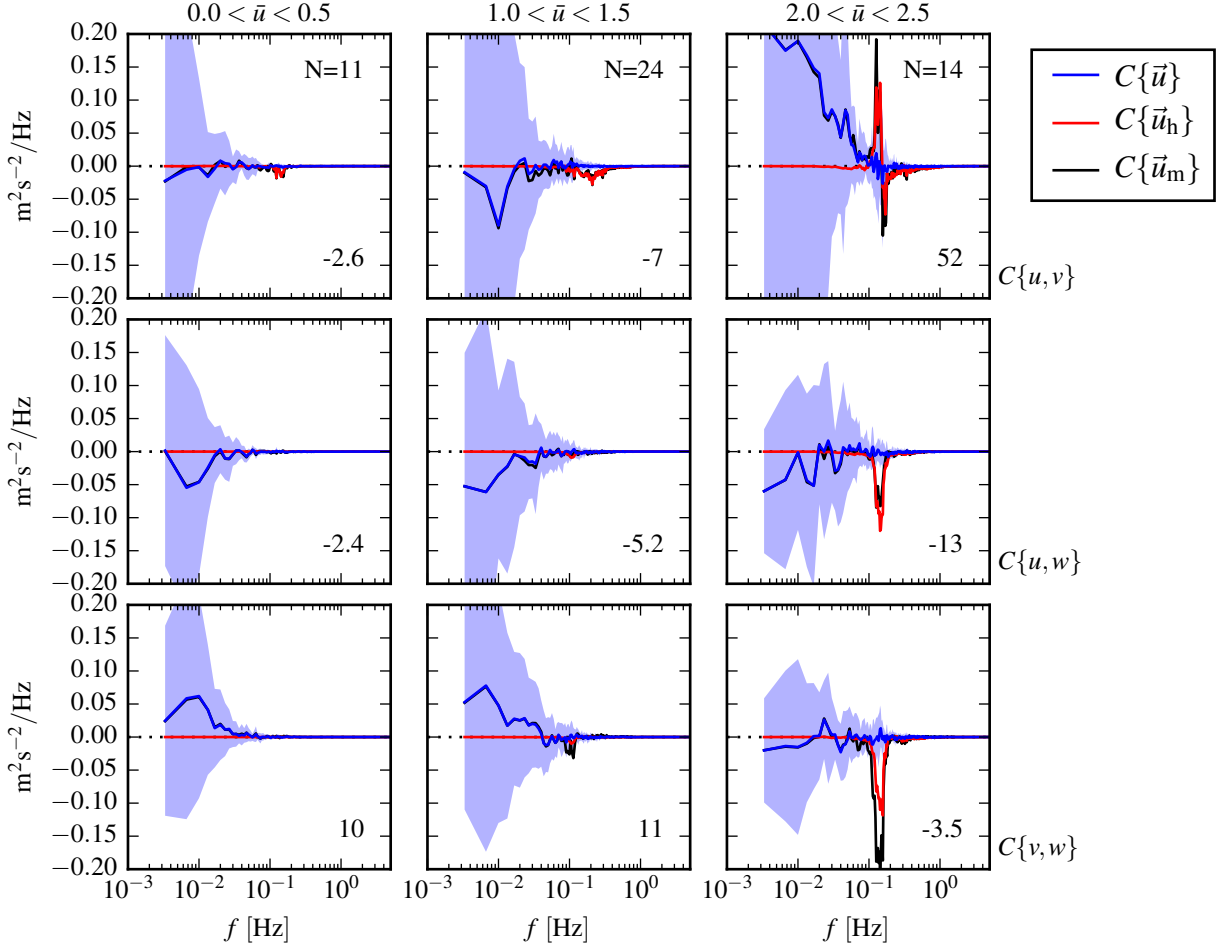


FIG. 11. The real part of the cross-spectral density between velocity components measured by the TTM. The upper-row is the u - v cross-spectral density, the middle-row is the u - w cross-spectral density, and the bottom-row is the v - w cross-spectral density. The columns are for different ranges of the stream-wise mean velocity magnitude (indicated above the top row). The blue line is the cross-spectrum between components of motion-corrected velocity, the red line is the cross-spectrum between components of head-motion, and the black line is the cross-spectrum between components of uncorrected velocity. The light-blue shading indicates one standard deviation of the C for the motion corrected cross-spectral density. N is the number of spectral ensembles in each column. The number in the lower right corner of each panel is the motion-corrected Reynold's stress (integral of the blue line) in units of $1\text{e-}4 \text{ m}^2 \text{s}^{-2}$.

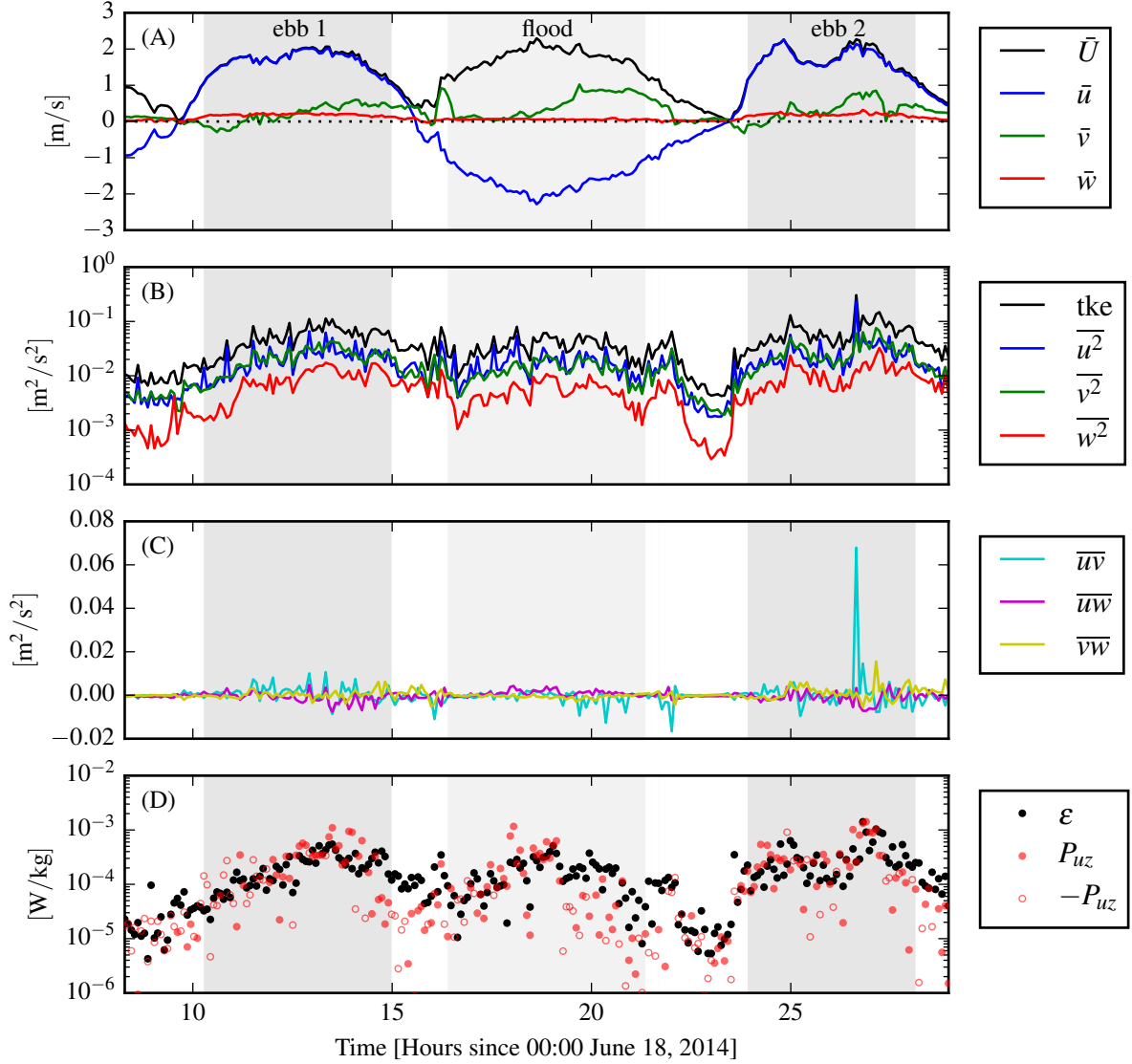


FIG. 12. Time-series of mean velocities (A), turbulence energy and its components (B), Reynold's stresses (C), and turbulence dissipation rate (D) measured by the TTM during the June, 2014 deployment. Shading indicates periods of ebb ($\bar{u} > 1.0$, grey), and flood ($\bar{u} < -1.0$, lighter grey).

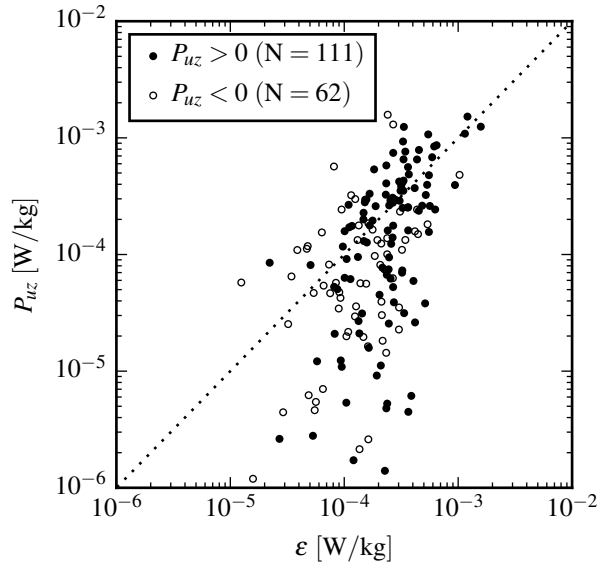


FIG. 13. P_{uz} vs. ε during the June 2014 TTM deployment for values of $|u| > 1$ m/s. Values of ‘negative’
production are indicated as open circles.

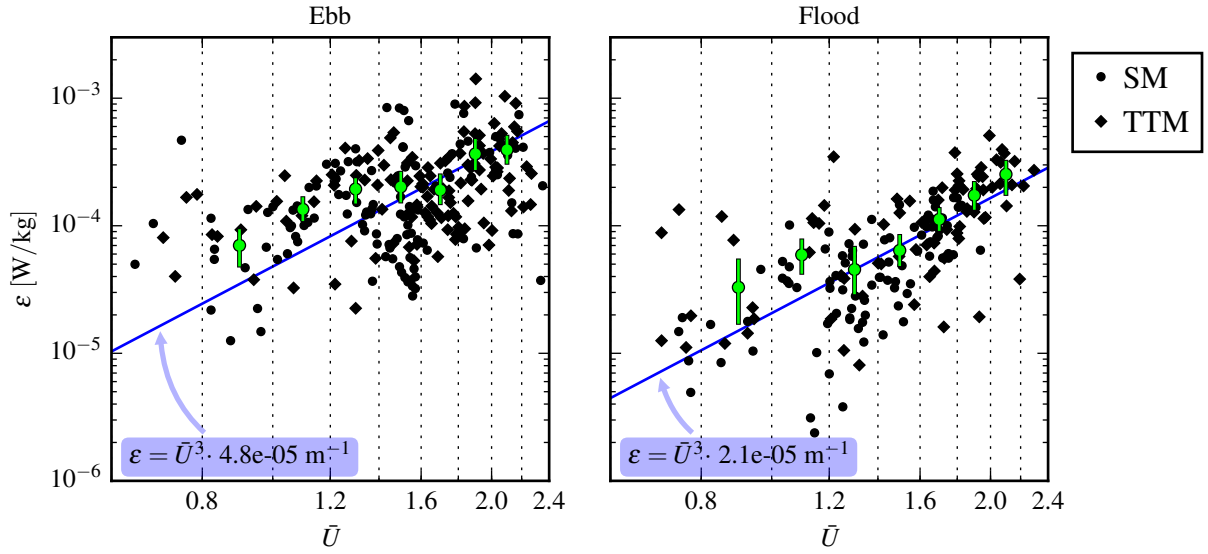


FIG. 14. A log-log plot of ε versus \bar{U} for the June 2014 TTM (diamonds) and May 2015 StableMoor (dots) deployments, during ebb (left) and flood (right). Black points are 5 minute averages. Green dots are mean values within speed bins of 0.2 m s^{-1} width that have at least 10 points (50 minutes of data); their vertical bars are 95% bootstrap confidence intervals. The blue line shows a U^3 slope, where the proportionality constant (blue box) is calculated by taking the log-space mean of ε/U^3 .

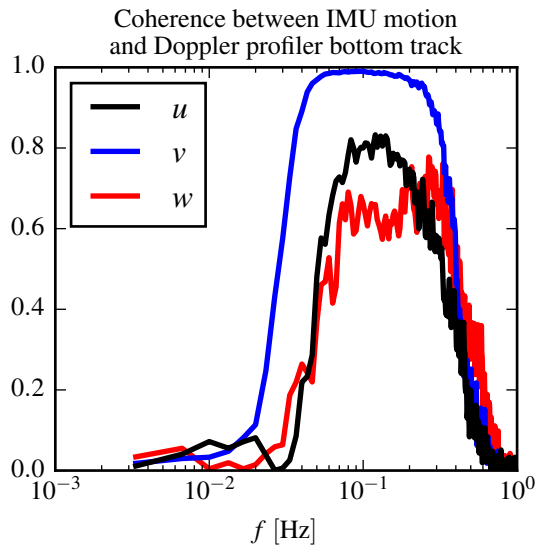


FIG. 15. Coherence between IMU-measured motion of StableMoor buoy and ADP bottom track velocity for $1.0 < \bar{U} < 1.5$. The vertical dotted line indicates the 95% confidence level for the 102 spectral windows in this estimate.